

Evidence for realignment of the charge density wave state in ErTe_3 and TmTe_3 under uniaxial stress via elastocaloric and elastoresistivity measurements

J. A. W. Straquadine,* M. S Ikeda, and I. R. Fisher

Geballe Laboratory for Advanced Materials and Department of Applied Physics, Stanford University, California 94305, USA

(Dated: May 22, 2020)

We report the evolution of a charge density wave (CDW) state in the quasi-2D rare-earth tritellurides ($R\text{Te}_3$ for $R=\text{Er},\text{Tm}$) as a function of in-plane uniaxial stress. Measurements of the elastocaloric effect, resistivity, and elastoresistivity allow us to demonstrate the importance of in-plane antisymmetric strain on the CDW and to establish a phase diagram. We show that modest tensile stress parallel to the in-plane a -axis can reversibly switch the direction of the ordering wavevector between the two in-plane directions. This work establishes $R\text{Te}_3$ as a promising model system for the study of strain-CDW interactions in a quasi-2D square lattice.

I. INTRODUCTION

Electronic correlations, especially in low-dimensional materials, give rise to a wide variety of charge ordered states, often in close proximity to other competing phases. Perhaps the most prominent example is the recent evidence for charge density wave (CDW) order in the cuprate superconductors [1–5]; the interplay between the CDW and superconducting states in these materials is currently a subject of debate. However, the interpretation of measurements of the charge order in materials such as the cuprates is made more complicated by the neighboring phases.

While the mechanisms driving CDW formation can be material-dependent[6–10], there is an overarching consensus that strong coupling between the electronic and lattice degrees of freedom is crucial.[11] As such, modifying the lattice with hydrostatic pressure, chemical pressure, or uniaxial stress can produce substantial changes in the CDW state.[12–16] The response of the CDW to such perturbations contains a wealth of information about the host material, ordered state, and the phase transition.

Of particular contemporary interest are layered materials which host in-plane unidirectional CDW states—such states break not just translational but also rotational symmetries. The component of the electronic order parameter that breaks rotational symmetry can then couple strongly to induced strains which break the same symmetry. In the presence of disorder, vestiges of the broken rotational symmetry may still persist despite a lack of true long-range phase coherence of the CDW correlations. This kind of “vestigial nematicity” has been proposed as an important component in the phase diagrams of a variety of strongly correlated materials[17–20]. However, such materials can also exhibit a wide range of competing or cooperating phases, which complicates the interpretation of experimental results. By identifying and studying model systems—that is, relatively simple materials in which the uniaxial CDW phase appears in

isolation or next to only a small number of other phases—one can gain a deeper understanding of CDW formation and the roles played by CDW fluctuations. Such studies can provide powerful guiding principles for further research into more complicated systems.

Uniaxial stress has emerged in recent years as a versatile tuning parameter for strongly correlated materials. Certain orientations of stress result in symmetry-breaking strains which can couple strongly to ordered phases which break similar symmetries. One can probe both the thermodynamic and transport behavior under strain using elastocaloric and elastoresistivity techniques, respectively. The elastocaloric effect—that is, the change in temperature under adiabatic changes in strain—provides insight into the effects of strain on the entropy landscape. Elastocaloric effect (ECE) measurements display similar singular behavior at phase transitions as other thermodynamic quantities such as the heat capacity. However, ECE measurements are selectively sensitive only to degrees of freedom which change due to strain, resulting in a much smaller background relative to the size of an anomaly at a phase transition.[21] Elastoresistivity, on the other hand, is defined as the normalized change in resistivity as a function of strain. As a transport technique, elastoresistivity (ER) probes strain-induced changes in the Fermi surface topology, density of states at the Fermi surface, and scattering processes such as critical fluctuations. The tensor describing the ER coefficients is fourth-rank, which is useful in discriminating a material’s response to strains belonging to different superimposed orthogonal symmetry channels.

The rare-earth tritelluride family of quasi-2D metals ($R\text{Te}_3$, $R=\text{La-Nd}, \text{Sm}, \text{Gd-Tm}, \text{Y}$) consist of bilayers of square Te nets separated by a buckled rock-salt layer of $R\text{Te}$, shown in Fig. 1(a). The crystal structure $R\text{Te}_3$ belongs to the orthorhombic space group $Cmcm$. (The standard crystallographic setting for this group defines the a and c axes as spanning the basal plane, with b normal to the plane.) The orthorhombicity arises due to a glide plane along the in-plane c -axis, which dictates the stacking of the $R\text{Te}$ slab layers and generates a slight difference in the two in-plane lattice parameters: $a \approx 0.999c$. For all R , the material undergoes a tran-

* jstraq@stanford.edu

sition to a unidirectional, incommensurate CDW phase with the wavevector $q_c \approx (0, 0, 2c^*/7)$. Chemical pressure tunes the transition temperature from above 500 K in LaTe_3 to 250 K in TmTe_3 . A second incommensurate CDW perpendicular to the first, with wavevector $q_a \approx (5a^*/7, 0, 0)$, appears for $R=\text{Tb, Dy, Ho, Er, Tm}$ at temperatures ranging from 41 K in TbTe_3 [22] to 180 K in TmTe_3 . Throughout this work, we denote the higher transition temperature as T_{CDW1} and the lower transition as T_{CDW2} .

In this paper, we report investigations of the effect of in-plane uniaxial stress on unidirectional CDW states in this material. Measurements of the resistivity, elastoresistivity, and elastocaloric effect of two representative members, ErTe_3 and TmTe_3 , as a function of temperature and stress all suggest an abrupt 90° in-plane realignment of the CDW wavevector under modest and practically accessible stresses, illustrated schematically in Fig. 1(f). Through this comprehensive study of the various phases and phase transitions, we establish $R\text{Te}_3$ as a promising model system for the study of strain-CDW interactions in a quasi-2D square lattice.

II. UNIDIRECTIONAL CDWS IN A QUASI-TETRAGONAL SYSTEM

Before describing our results in this specific model system, it is instructive to consider the general expectations based on a phenomenological free energy expansion. Consider a two-dimensional system with tetragonal symmetry which supports incommensurate unidirectional CDW order along both the a - and c -axes, where we keep the notation of a and c as in-plane lattice parameters for immediate comparison to $R\text{Te}_3$.

Following the seminal work of McMillan[23], but using the crystallographic coordinates of $R\text{Te}_3$, we take as our order parameters

$$\psi_i(\mathbf{r}) = \psi_{i0}(\mathbf{r})e^{i\mathbf{q}_i \cdot \mathbf{r}} \quad (1)$$

where $i = a, c$, and the subscript 0 is used to indicate the absence of applied stress. Knowledge of the $R\text{Te}_3$ family allows us to make several simplifying assumptions. First, the Fourier expansion coefficients should in principle be treated as periodic functions of space with the periodicity of the lattice. However, the smooth variation of \mathbf{q}_c and \mathbf{q}_a with temperature[22, 24, 25] suggests an absence of commensurability effects. Crystals of $R\text{Te}_3$ are also relatively free of disorder which can locally pin the CDW phase, as observed in x-ray diffraction[22, 25], STM[26–28], electrical transport[29, 30] and quantum oscillations[16, 31, 32]. This allows us to treat the wavevectors \mathbf{q}_a and \mathbf{q}_c as fixed, spatially uniform parameters. Finally, the orthogonality of the two wavevectors ensures that in the absence of pinning potentials and higher order non-linear effects the phases of the order parameters $\psi_a(\mathbf{r})$ and $\psi_c(\mathbf{r})$ are mutually independent. These assumptions together allow us to consider only the

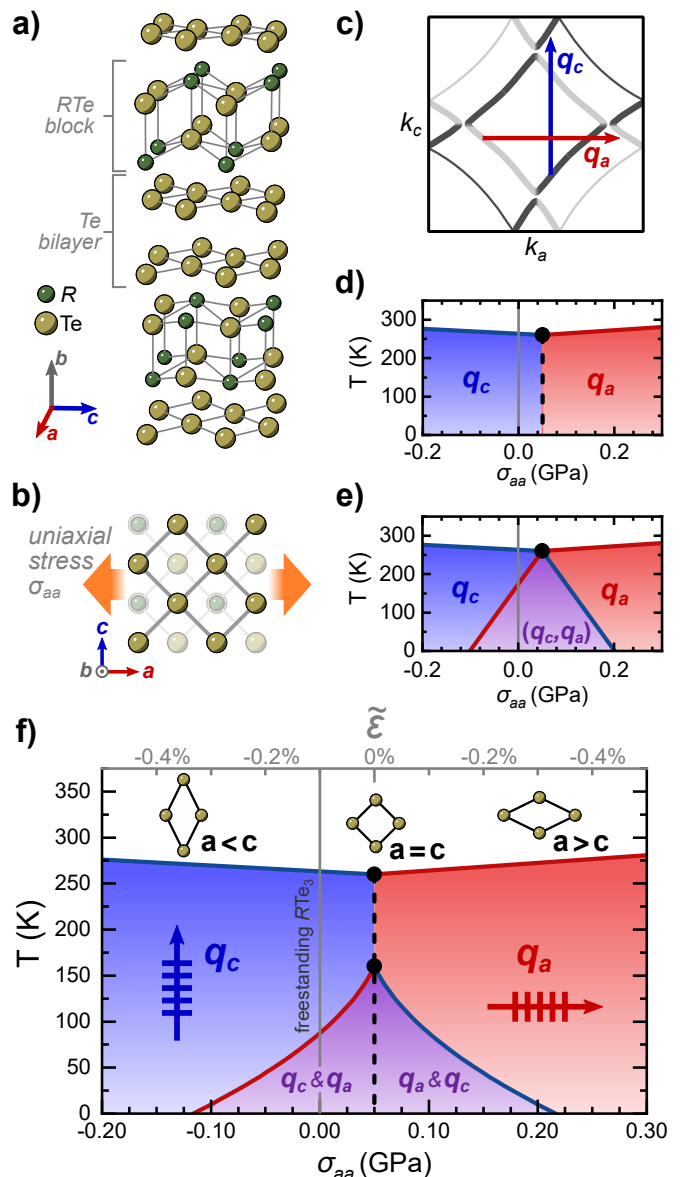


FIG. 1. (a) Crystal structure of $R\text{Te}_3$. The stacking of the $R\text{Te}$ block layers produces a glide plane which breaks C_4 symmetry. (b) Crystal structure viewed along the out-of-plane b -axis. The c -axis is 0.1% longer than the a -axis, and uniaxial tensile stress along a can invert the orthorhombic distortion. (c) Schematic of the Fermi surface of $R\text{Te}_3$, showing the two orthogonal CDW ordering vectors. This is the result of a tight-binding model for a single plane, neglecting the effects of b -axis dispersion and bilayer splitting, both of which are small. The CDW vectors approximately nest large regions of the Fermi surface. (d) Temperature-uniaxial stress phase diagram described by Eq. (2) for $g > 0$. Solid lines indicate continuous phase transitions, and dashed lines indicate first order transitions. The stress axis is defined relative to a free-standing orthorhombic $R\text{Te}_3$ crystal. (e) Phase diagram of Eq. (2) for $g < 0$. A region of coexisting CDW order with both wavevectors opens at low temperatures, and all transitions are continuous. (f) Phase diagram of Eq. (6) incorporating higher order terms, which captures the phenomenology observed in thermodynamic and transport under uniaxial stress. Both the first order transition and the coexistence region are preserved. Coefficients appropriate for ErTe_3 are used in calculating (d)-(f).

CDW gap magnitudes and suppress any gradient terms in our free energy expansion. For brevity, from this point forward we use the notation $\psi_a = |\psi_a|$, $\psi_c = |\psi_c|$.

As we introduce stress and strain terms into our free energy, we must also make a distinction between this idealized tetragonal model and the realistic orthorhombic structure of $R\text{Te}_3$. We define the strain ε_{ij} and stress σ_{ij} tensors relative to the $R\text{Te}_3$ crystal; $\varepsilon_{ij} = 0$ and $\sigma_{ij} = 0$ for a freestanding sample. We add a tilde ($\tilde{\varepsilon}_{ij}$, $\tilde{\sigma}_{ij}$) to denote strain and stress defined such that $\tilde{\varepsilon}_{ij} = 0$ and $\tilde{\sigma}_{ij} = 0$ corresponds to the ideal tetragonal case. The orthorhombicity of $R\text{Te}_3$ can be accounted for by a weakly temperature-dependent offset: $\varepsilon_{ij} + \varepsilon_{ij}^0 = \tilde{\varepsilon}_{ij}$, $\sigma_{ij} + \sigma_{ij}^0 = \tilde{\sigma}_{ij}$.

Furthermore, we choose a basis for the stress, strain, and elastic constant tensors motivated by tetragonal symmetry, using the subscripts A and S for antisymmetric and symmetric in-plane components, respectively: $\tilde{\varepsilon}_A = (\tilde{\varepsilon}_{cc} - \tilde{\varepsilon}_{aa})/2$, $\tilde{\varepsilon}_S = (\tilde{\varepsilon}_{cc} + \tilde{\varepsilon}_{aa})/2$, and similar for the stresses $\tilde{\sigma}_A$ and $\tilde{\sigma}_S$. Analogous stress and strain terms can be defined in the orthorhombic reference frame as well (e.g. $\varepsilon_A = (\varepsilon_{cc} - \varepsilon_{aa})/2$), however it should be noted that the subscripts A and S do not formally correspond to antisymmetric and symmetric strains; in the absence of tetragonal symmetry, these are no longer independent basis functions for different irreducible representations of the point group. The elastic constants of both the tetragonal model and orthorhombic $R\text{Te}_3$ are assumed to be equivalent. In this basis, neglecting contributions from out of the plane, the symmetrized and antisymmetrized elastic constants are defined as $\tilde{C}_S \approx C_S = 2(C_{aaaa} + C_{aacc})$ and $\tilde{C}_A \approx C_A = 2(C_{aaaa} - C_{aacc})$, where the factor of two is added for convenience, simplifying terms in the associated free energy after performing the necessary Legendre transformation.

Taking the tetragonal case as a reference, consider an expansion to fourth order in ψ_a and ψ_c of the Gibbs free energy (constant stress, constant temperature) given by:

$$G_4 = G_\psi + G_\varepsilon + G_c \quad (2)$$

$$G_\psi = \frac{a_0 t}{2}(\psi_a^2 + \psi_c^2) + \frac{b}{4}(\psi_a^2 + \psi_c^2)^2 + \frac{g}{2}\psi_a^2\psi_c^2 \quad (3)$$

$$G_\varepsilon = \frac{\tilde{C}_A}{2}\tilde{\varepsilon}_A^2 + \frac{\tilde{C}_S}{2}\tilde{\varepsilon}_S^2 - 2(\tilde{\sigma}_A\tilde{\varepsilon}_A + \tilde{\sigma}_S\tilde{\varepsilon}_S) \quad (4)$$

$$G_c = \lambda\tilde{\varepsilon}_A(\psi_c^2 - \psi_a^2) + \eta\tilde{\varepsilon}_S(\psi_c^2 + \psi_a^2) \quad (5)$$

where $t = (T - T_c^0)/T_c^0$ is the reduced temperature and T_c^0 is the critical temperature in a freestanding crystal. Translational symmetry prevents the existence of bilinear terms involving the order parameters; the λ and η terms are the lowest order couplings allowed. The coefficients a_0 , b as well as the elastic constants C_S and C_A must be positive. Empirically, we note that the upper transition T_{CDW1} corresponds to the formation of a CDW state with a wavevector parallel to the longer c -axis. Therefore the coupling constant λ between the antisymmetric strain and the order parameters must be negative. This is also supported by measurements of the

thermal expansion below T_{CDW1} [25]. Hydrostatic pressure experiments[12, 15, 16] suggest that the symmetric coupling coefficient η must also be negative. The phase diagram produced by this model for a few sets of coefficients are shown in panels (d) and (e) in Fig. 1.

The orthorhombic crystal structure (specifically the ab and bc mirror planes which contain the CDW wavevectors) precludes such an elastic coupling between the order parameters and in-plane shear strain. The lowest order coupling terms between the order parameters and shear terms ε_{ab} , ε_{bc} , and ε_{ac} are biquadratic and are neglected here.

Previous work has explored the $R\text{Te}_3$ phase diagram with the assumption of C_4 symmetry without strain coupling[33], equivalent to the case $\lambda = \eta = 0$. In this case, g must be positive in order for a unidirectional CDW to form rather than a checkerboard state. Reintroducing the stress coupling, we then see that antisymmetric stress can be expected to train the CDW wavevector between the \mathbf{q}_c and \mathbf{q}_a states, which are separated by a first order transition as shown in Fig. 1(d). In such a model, no second CDW transition is observed at lower temperatures. This would appropriately describe the phase diagram of $R\text{Te}_3$ for $R=\text{La, Ce, Pr, Nd, Sm, and Gd}$.

The case for $g < 0$, considered in Fig. 1(e), exhibits similar wavevector switching behavior but produces a finite region of coexistence of both the \mathbf{q}_c and \mathbf{q}_a states, bounded by a pair of second order transitions. At first glance, a vertical cut of this phase diagram for finite $\tilde{\sigma}_A$ appears to reproduce the cascade of phase transitions observed in $R\text{Te}_3$ for $R=\text{Tb, Dy, Ho, Er, and Tm}$. However, later sections of this work will demonstrate that the character of the observed phase transitions is incompatible with $g < 0$: we find that the strain-induced transition between \mathbf{q}_c and \mathbf{q}_a is indeed first order, as indicated in Fig. 1(d).

Reproducing the proper topology of the phase diagram for the heavy rare earth compounds requires the inclusion of higher order terms. One such model has been explored to 8th order for the case of $R\text{Te}_3$ in the presence of disorder[34]. In the pristine case, we have found that adding the two possible sixth order terms Eq. (2) suffices to capture the basic phenomenology of our observations:

$$G = G_4 + r(\psi_c^2 + \psi_a^2)^3 + \gamma(\psi_c^4\psi_a^2 + \psi_c^2\psi_a^4) \quad (6)$$

where $g > 0$, $r > 0$, and $\gamma \approx -r/2$. This phase diagram is shown in Fig. 1(f).

III. EXPERIMENTAL METHODS

Uniaxial stress was generated using a commercially available stress cell, specifically the CS-100 from *Razorbill Instruments*, in which a bar-shaped sample was attached spanning a pair of mounting plates, shown schematically in Fig. 2. The sample was then stressed by changing the spacing of the mounting plates *in situ* by

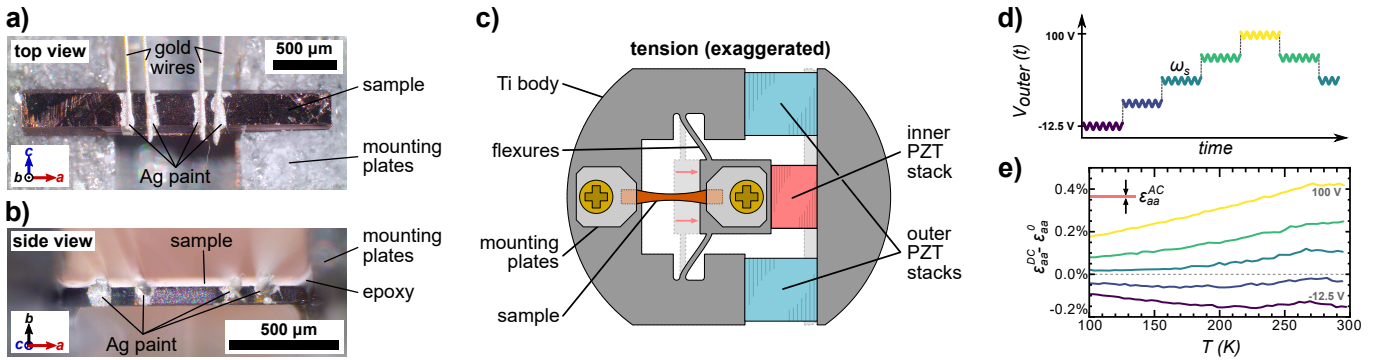


FIG. 2. Description of the experimental setup. (a) Microscope photograph of the top and (b) side view of a representative ErTe_3 sample mounted in the stress cell, and contacted for a -axis resistivity and elastoresistivity measurements. (c) Cartoon drawing of the CS-100 stress cell from *Razorbill Instruments*. The outer two piezoelectric actuators were elongated ($V_{\text{outer}} > 0$) and the inner is compressed ($V_{\text{inner}} < 0$), resulting in tensile stress applied to the sample. (d) Schematic of the voltage applied to the outer stacks as a function of time. The actuator voltage was the sum of a stepwise DC offset (ca. -25 - 100 V) with a small sinusoidal oscillation (ca. $5 V_{\text{rms}}$, 30 - 80 Hz). Data was taken continuously while the sample temperature was ramped slowly (approx. 1 K/min), and the duration of each DC step was approximately 6.5 seconds. (e) DC component of the strain measured for a representative ErTe_3 sample as a function of temperature and offset voltage V_{outer} . The temperature dependent response of the piezoelectric actuators contributes to some drift in strain for any given temperature. The height of the shaded bar in the upper left corner of (e) represents the maximum amplitude of the AC strain oscillation which was superimposed on this data.

applying voltages to three piezoelectric actuators (made of stacks of lead zirconate titanate, or PZT). The outer two stacks were connected in parallel to a single voltage V_{outer} , and elongation produced tensile stress. Elongation of the inner stack (V_{inner}) generates compressive stress. This experimental design minimized effects due to thermal expansion of the PZT. The crystal changes shape due to the stress that it experiences, but we measured the resulting strain rather than the stress. Certain caveats associated with this are described below.

The measurements described in this work required the superposition of both static and oscillating stresses. We generated a waveform of $V_{\text{outer}} = V_{\text{dc}} + V_{\text{ac}} \cos(2\pi f_s t)$ to drive the outer PZT stacks, and a separate static voltage V_{inner} was applied to the inner stack. V_{dc} varied between -25 V and 100 V, f_s varies between 20 Hz and 90 Hz, and an oscillation of $5 V_{\text{rms}}$ was used for all measurements. Uniaxial stress was applied primarily in tension, to avoid buckling or delaminating these soft, layered samples.

In order to disentangle effects which rely on the temperature and strain history of the sample, data were collected using two different protocols. The first was to slowly sweep temperature while stepping V_{outer} up and down. On each step, the DC component was changed by ± 12.5 V. Unless otherwise noted, data presented in the figures only shows data taken for steps which were increasing in voltage although data was also taken for decreasing steps. The cases of increasing and decreasing voltages differ by a slight hysteresis ascribed to the first order transition, but otherwise show the same qualitative behavior.

The second protocol used was to sweep temperature up and down for a fixed value of V_{dc} . It should be noted that this is not equivalent to measurement at constant strain.

While the strain was monotonic in V_{dc} at any given temperature, temperature dependence of the displacement per volt in the PZT actuators caused the actual strain to drift as a function of temperature, as shown in Fig. 2(e).

The displacement ΔL of the jaws was measured using the capacitive sensor built into the CS-100 cell. We used a custom-built autobalancing bridge circuit to convert the capacitance to a voltage signal, which was then interrogated with standard lock-in amplifiers. This circuit enabled accurate detection of both the constant displacement offset as well as the oscillating component (for strain frequencies up to 1 kHz), and is described in detail in appendix A.

In an ideal case, where the stress cell and epoxy would be infinitely stiff compared to the sample, the sample strain is given by $\varepsilon = \Delta L/L$, where L is the sample length and ΔL is the displacement detected by the capacitive sensor. This case would be equivalent to the thermodynamic condition of fixing constant strain along the long axis of the sample (temporarily defining this as the x -axis ε_{xx}) while the other components of the strain tensor are allowed to relax. This differs slightly from the conditions described in the guiding model of the previous section, in which $\bar{\sigma}_{xx}$ was held constant. In a free-standing crystal, the coupling terms between the CDW and strain (λ and η in Eq. (5)) cause strain to behave like a secondary order parameter. A finite value of the CDW gap in either direction induces a sympathetic orthorhombic distortion. Fixing constant strain rather than stress would largely preserve the phase diagram of Fig. 1(f) except near the \mathbf{q}_a - \mathbf{q}_c transition—the first order transition would widen to encompass a region characterized by a patchwork of orthogonal domains of $|\tilde{\varepsilon}_A| > 0$ such that the average strain matched the externally imposed condition. In re-

ality, however, we must mention three caveats regarding this idealized constant-strain condition.

First, the pliability of the epoxy is known to decrease the strain transmitted to the sample. Simulations for the case of iron-pnictide superconductor samples show strain transmission of approximately 70% the ideal value[35]. This effect changes quantitative estimates of critical values of the strain to induce the phase transition shown in Fig. 1(f), but does not affect the overall features of the phase diagram. For the present study we therefore neglect this effect since our focus is on general features of the strain-tuned phase diagram. Secondly, mismatch of the thermal expansion coefficients between the sample and titanium cell body generates a temperature-dependent stress. In the case of $R\text{Te}_3$, the in-plane thermal expansion is approximately five times larger than that of titanium at room temperature[25]. While the thermal expansion of $R\text{Te}_3$ has not been measured for all temperatures, it is sensible to assume that the estimated magnitude of tensile (compressive) strain is always underestimated (overestimated). We incorporate the contraction of titanium in our estimate of the jaw spacing L , but we do not apply any correction for thermal expansion of the sample. Finally, the process of curing the mounting epoxy can produce built-in strains even at room temperature, and this offset varies from sample to sample. In order to compare samples on the same scale, we extract the location of the critical point between the \mathbf{q}_c , \mathbf{q}_a , and disordered states, which we define as occurring at the degeneracy strain ε_{aa}^0 . The arguments provided in this paper do not require the exact knowledge of the absolute strain, but rather focus on the relative changes.

Single crystals of ErTe_3 and TmTe_3 are grown by a self-flux method described elsewhere.[29] The in-plane a - and c -axes are distinguished using x-ray diffraction by comparing amplitudes of the (061) peak with its forbidden counterpart (160). Samples are cleaved and cut by hand with a scalpel into rectangular bars of 1.3–2.4 mm in length, 250–500 μm in width, and 25–130 μm in thickness. The sample is then epoxied and clamped to the stress cell between a set of roughened titanium mounting plates. The sample is electrically isolated from the bottom titanium mounting plates with small pieces of thin tissue paper impregnated with epoxy. The distance between the edges of the clamps is approximately 1 mm.

We detect strain-induced oscillations in the sample temperature using a thermocouple. A Type E thermocouple is formed by spot-welding pieces of constantan and chromel thermocouple wire, both 12.5 μm in diameter. The welded junction is then attached to the center of the top face of the sample using either two-part epoxy or silver paint. While the phenomenology is the same, we found slightly better thermal coupling between the thermocouple and sample when using silver paint. The reference junction is formed by attaching the free ends of the wires to copper pads which are thermalized to (but electrically isolated from) the body of the strain cell, as in ref. 36. The detected signal is amplified with an SR554

transformer as well as an SR580 preamplifier, together providing a composite gain of 2000.

Electrical contacts are formed by selectively sputtering gold onto desired regions of the freshly cleaved surface, and gold wires are attached with *DuPont* 4929 silver paint. All of the contacts are placed within the suspended section of the crystal to minimize contributions from the clamped regions, which may experience significant strain inhomogeneity. The resistivity and elastoresistivity are extracted using the demodulation techniques presented in [37]. The voltage signal is amplified through an SR554 transformer from *Stanford Research Systems* with gain of 100. The transformer’s frequency dependence is independently calibrated and measured signals are corrected to reflect this.

IV. RESULTS

A. Elastocaloric effect measurements

The elastocaloric effect (ECE) reflects the strain-dependence of the entropy of a material. The ECE can refer either to the change in entropy resulting from isothermal changes in strain $(dS/d\varepsilon)_T$ or to the change in temperature resulting from an adiabatic change in strain: $(dT/d\varepsilon)_S$. We use the latter definition throughout this work. The ECE relates both to critical fluctuations near a strain-tuned transition, as well as equilibrium thermodynamic quantities such as the heat capacity and thermal expansion, as will be described in detail in Section V. The elastocaloric effect (ECE) in ErTe_3 under uniaxial stress, measured while slowly cooling and stepping the PZT control voltage up and down, is presented in Fig. 3. Similar data for TmTe_3 are shown in Fig. 4. In both figures, panel (a) corresponds to stress parallel to the a -axis. In this orientation, a step-like anomaly appears at T_{CDW1} , which is approximately 265 K for ErTe_3 . For slightly compressive stresses (negative V_{outer}), the anomaly at T_{CDW1} causes the ECE to increase in magnitude upon cooling through the transition. The magnitude of the step decreases with increasing tensile strain, and eventually the step inverts and the ECE decreases in magnitude upon cooling through T_{CDW1} . Further increasing the tensile stress causes the step to grow again in magnitude until it saturates. At the largest tensile strains, the transition into the CDW state corresponds to an $\approx 85\%$ decrease of the total ECE signal.

As a thermodynamic probe, the ECE is expected to display a cusp at the critical temperature, similar to the heat capacity.[21] We identify this feature, and therefore T_{CDW1} , as an extremum in the second derivative of the ECE with temperature, which removes bias due to the background. The extracted values are plotted in panel (b) of Fig. 3. We define ε_{aa}^0 as the strain for which T_{CDW1} reaches a minimum, corresponding to $\tilde{\varepsilon}_A = 0$ in Section II. This point also then corresponds to where $dT_{CDW1}/d\varepsilon$ changes sign, as well as where the step-like anomaly flips

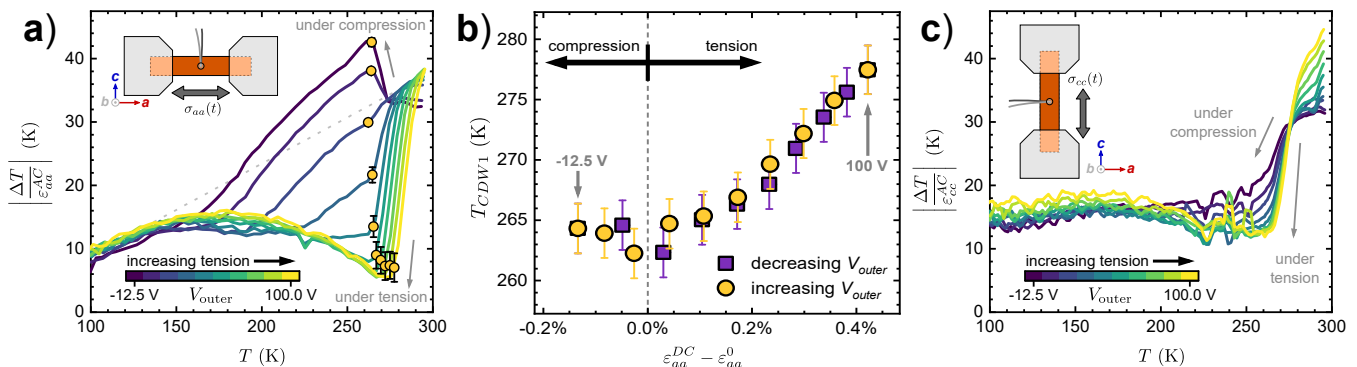


FIG. 3. Elastocaloric effect results for a sample of ErTe_3 with uniaxial stress (a) Magnitude of the elastocaloric response with stress parallel to the a -axis as a function of temperature and offset voltage. The critical temperature T_{CDW1} (circles) is extracted from an extremum in the second derivative. Inset: schematic of the experimental setup. The dotted line is a guide to the eye for a linear background independent of strain. The anomaly at T_{CDW1} rises above this background for compressive stresses, but changes sign for large enough tensile strain. (b) Critical temperatures T_{CDW1} extracted from (a) as a function of DC offset strain, shown for both increasing and decreasing PZT voltage steps. The critical temperature rises as one departs from ε_{aa}^0 toward either compressive or tensile strain. (c) Elastocaloric effect with stress parallel to the c -axis. Tension increases the magnitude of the critical anomaly, but no switching behavior is observed.

its direction.

Such switching behavior is not observed when tensile stress is applied parallel to the c -axis, as seen for ErTe_3 in Fig. 3(c). In contrast to the elastocaloric effect for a -axis stress, even the most compressive traces correspond a decrease in ECE magnitude cooling through T_{CDW1} . Additionally, similar to the case for the strain-induced \mathbf{q}_a stripe state, increasing tensile strain slightly increases T_{CDW1} . The resemblance between the elastocaloric effects observed for c -axis stress and the limit of high tensile a -axis stress further suggests that the CDW flop preserves the qualitative structure/characteristics of the CDW with the exception of a 90° rotation. For $T \lesssim T_{CDW2}$ the ECE curves again become largely independent of both the orientation and magnitude of the stress.

ECE measurements in TmTe_3 for a -axis strain, shown in Fig. 4, follow the same trends as ErTe_3 . Cooling through T_{CDW1} (≈ 245 K) increases the ECE under compressive stress, and decreases under tensile stress. The extracted critical temperature also exhibits a weak minimum, with a stronger increase for the largest tensile strains. The response on the compressive side is mostly flat, which we attribute to buckling of the sample. Buckling would imply poorer transmission of the measured strain into the sample, which is consistent with the smaller ECE signal observed for the most compressive case, $V_{\text{outer}} = -12.5$ V.

The data presented in Fig. 4 was taken under conditions of temperature sweeps with constant PZT control voltages. This dataset, in conjunction with the ErTe_3 data in Fig. 3, demonstrate that the qualitative features do not depend on the stress and temperature history.

B. Resistivity

As a direct probe of quasiparticles at the Fermi level, electrical transport is highly sensitive to the opening of CDW gaps. The resistive signatures of both CDW transitions are most clear in the out-of-plane component ρ_{bb} , which averages roughly equally over the entire quasi-2D FS. Out-of-plane resistivity measurements in ErTe_3 under a -axis stress are presented in Fig. 5. T_{CDW1} and T_{CDW2} are identified as minima in the temperature derivative.

T_{CDW1} shows the same trend as evinced from elastocaloric measurements—a minimum for a small amount of tensile stress with increases on either side. The height of the resistivity bump below T_{CDW1} , which is related to changes in the density of states the Fermi level due to the opening of the CDW gap, decreases only slightly. This indicates that despite the large change in behavior of the ECE signal under stress, a gap of similar magnitude appears to open regardless of the stress. Measurements of ρ_{bb} alone, however, do not provide information on which sections of the quasi-2D Fermi surface become gapped.

As the tensile strain increases, we see that T_{CDW2} decreases significantly, dropping ≈ 20 K for strains of 0.1%. Simultaneously, the corresponding bump in resistivity decreases in magnitude as well. Unlike T_{CDW1} , T_{CDW2} decreases monotonically with increasing tensile strain. We attribute this to an unmeasured strain offset arising from mismatched thermal expansion between the Ti stress cell and the sample. The contraction of the sample on cooling relative to the stress cell implies that the sample has drifted toward positive tensile stress as the temperature decreased. The monotonic decrease in T_{CDW2} suggests that the stress is, at these temperatures, beyond that required to realign the primary wavevector by 90° .

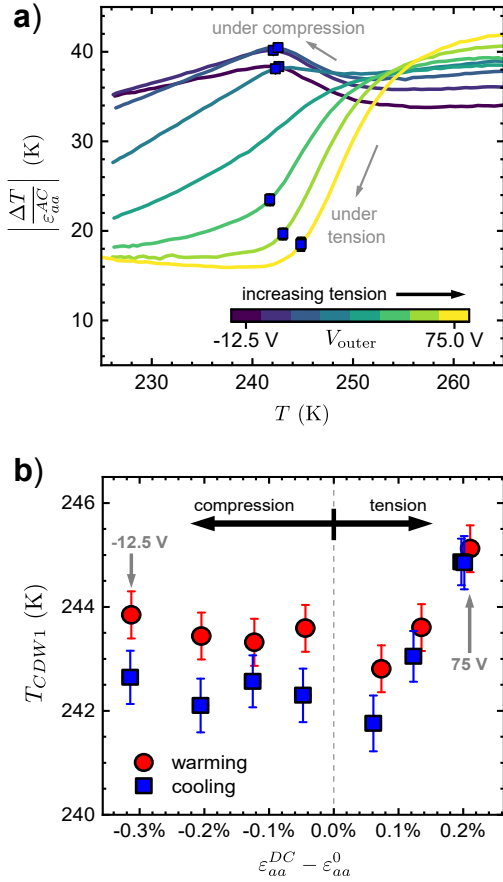


FIG. 4. Elastocaloric effect measurements in TmTe_3 with stress parallel to the a -axis. (a) Magnitude of the elastocaloric response near T_{CDW1} as a function of temperature and PZT voltage. Each trace was collected by cooling at a constant V_{outer} , and T_{CDW1} is extracted by the second derivative. Despite using different data acquisition protocols and different rare earths, the results in Fig. 3 share the same behavior. (b) Extracted critical temperatures on the same sample for both warming and cooling traces. The increase of T_{CDW1} for tensile strains is clearly defined, although an increase on the compressive side is not observed. We attribute this to slight buckling of the sample, resulting in an overestimate of the compressive strain. One of the curves near the center exhibited no clear extremum in the second derivative, so T_{CDW1} could not be unequivocally identified. Tension and compression are labeled (black arrows) relative to $\tilde{\epsilon}_A = 0$.

The in-plane resistivity components, ρ_{aa} and ρ_{cc} , are presented in Fig. 6 for ErTe_3 . These components show similar features at the CDW transitions, but also provide insight into the anisotropy of the Fermi surface in the ordered phases. In particular, it has previously been established[30, 38] that the CDW gap with wavevector \mathbf{q}_c has a larger effect on ρ_{aa} than on ρ_{cc} , and vice versa. This is also observed clearly in the top panel of Fig. 6 for a freestanding sample. Switching of the CDW wavevector from \mathbf{q}_c to \mathbf{q}_a would then be accompanied by a change in the relative magnitude of the anomalies at T_{CDW1} and

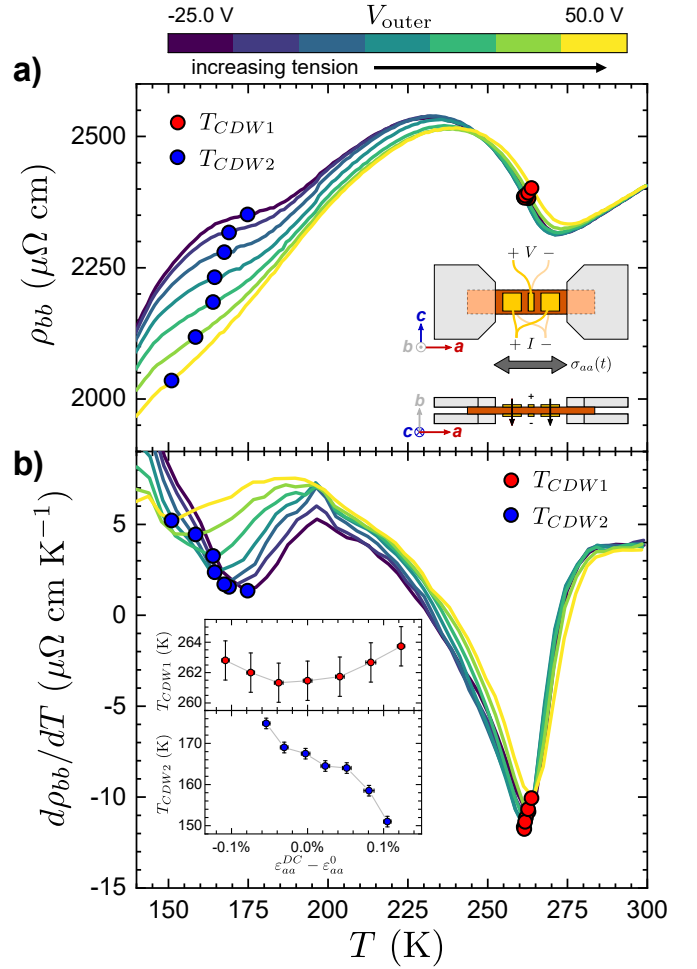


FIG. 5. Out-of-plane resistivity ρ_{bb} in ErTe_3 . Panel (a) shows the resistivity traces for a series of PZT voltages. Inset: top and side view schematics of the contact geometry used in this experiment. Current is passed into the sample through the larger, outer two contacts on both the top and bottom of the crystal, and the smaller center pads are used to detect the voltage. Temperature derivatives of the resistivity traces are shown in panel (b). The minima of the derivative traces correspond to the critical temperatures. Inset to (b): T_{CDW1} and T_{CDW2} plotted as a function of strain. The lack of a maximum in T_{CDW2} corresponding to the minimum in T_{CDW1} and the switch between the two cases is attributed to an underestimate of the tensile stress arising from mismatched thermal expansion of the sample and stress cell.

T_{CDW2} . This is exactly what is observed.

The lower two panels in Fig. 6 show longitudinal measurements of both $\rho_{aa}(\epsilon)$ and $\rho_{cc}(\epsilon)$ under uniaxial stress parallel to the current flow. For slightly compressive a -axis stress, $\rho_{aa}(\epsilon)$ closely resembles the freestanding value, $\rho_{aa}(\epsilon = 0)$. As σ_{aa} increases, however, the effect of T_{CDW1} decreases in magnitude, and $\rho_{aa}(\epsilon_{aa})$ eventually crosses over to behave like $\rho_{cc}(\epsilon = 0)$ instead. The switch between the two limits occurs gradually as a function of stress.

In contrast, no such switching behavior is seen in

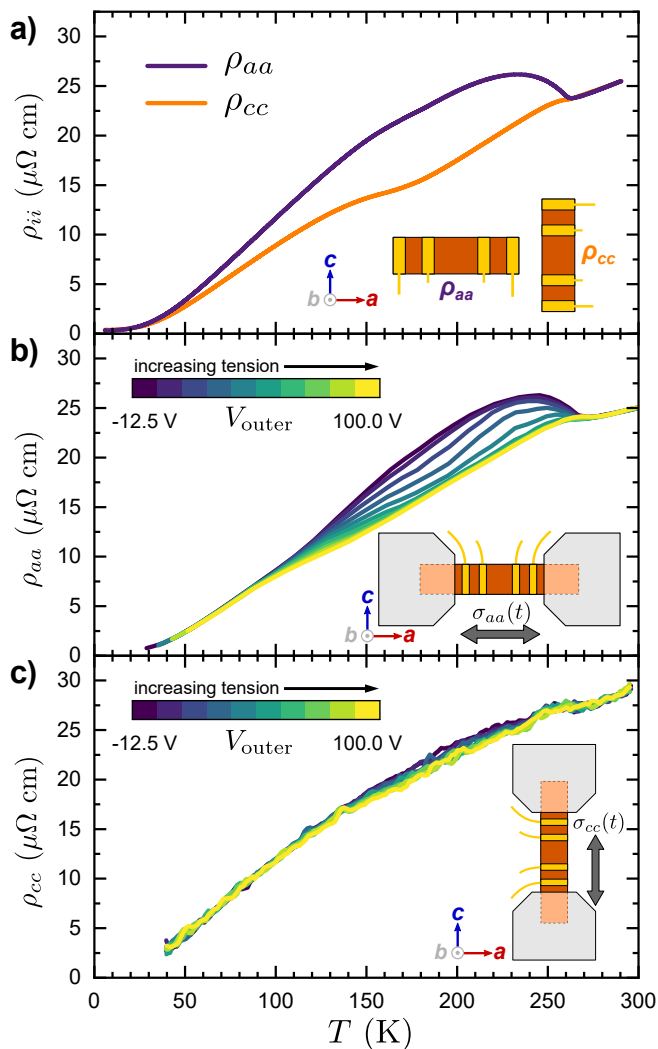


FIG. 6. In-plane resistivity components of ErTe₃ as a function of temperature and strain. (a) free-standing resistivity components of ErTe₃. Resistivity along the a -axis increases more strongly upon entering the \mathbf{q}_c state due to the curvature of the gapped region of the Fermi surface[30]. (b) a -axis resistivity of ErTe₃ under a -axis stress, as a function of temperature and PZT voltage. Negative and low voltages behave similarly to the freestanding case for ρ_{aa} , but crosses over to resemble freestanding ρ_{cc} as the tension increases. (c) c -axis resistivity under c -axis stress, which does not demonstrate any switching behavior.

$\rho_{cc}(\varepsilon)$. A slight decrease of the resistivity can be observed for the largest tensile stresses, but the curves never deviate very far from $\rho_{cc}(\varepsilon = 0)$. On general grounds, tensile σ_{cc} will reinforce the intrinsic orthorhombicity of the material. Tensile σ_{aa} opposes this orthorhombicity, however, and will train the CDW wavevector along \mathbf{q}_a in the model presented in Section II. In principle compressive σ_{cc} would have a similar effect, but as mentioned in Section III the soft RTe₃ samples are prone to buckling under compression, so this regime is not accessible

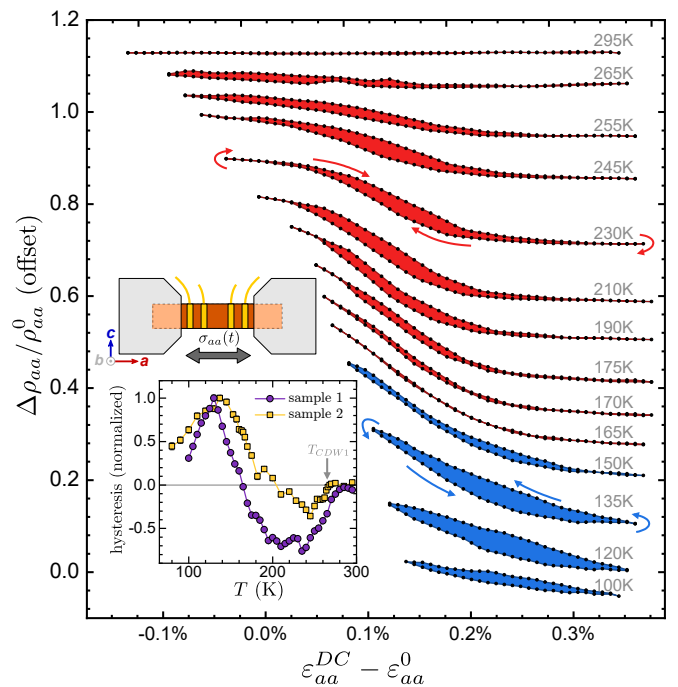


FIG. 7. Ratiometric change in ρ_{aa} of ErTe₃ through stress cycles performed at a few representative temperatures. Curves are offset vertically for clarity. Inset: Schematic of the contact and stress geometry, and plot of the integrated area contained within the hysteresis loops in (b) for two different samples of ErTe₃. In both, the hysteresis loops open as the sample cools through T_{CDW1} . The hysteresis loop changes direction (clockwise to counterclockwise) as the temperature decreases further. The extracted area is sensitive to the exact DC strain range accessed, which accounts for the differences between samples. The observed hysteresis clearly indicates the first-order nature of the phase transition where the direction of the CDW wavevector switches from \mathbf{q}_a to \mathbf{q}_c , corresponding to the schematic phase diagram shown in Fig. 1(f).

here. In summary, the observed behavior of both $\rho_{aa}(\varepsilon)$ and $\rho_{cc}(\varepsilon)$ appears consistent with a reorientation of the CDW wavevector from \mathbf{q}_c in the freestanding crystal to \mathbf{q}_a under a -axis tensile strain.

In order to examine the character of this reorientation transition, we have performed σ_{aa} stress cycles on a sample of ErTe₃ at constant temperature while measuring the a -axis resistivity. The results of these measurements are presented in Fig. 7. Above T_{CDW1} , very little strain-induced change in the resistivity is observed. As the sample cools below T_{CDW1} , a clear hysteresis loop opens and increases in area. The exact size and shape of the hysteresis loops depends on the extent of the stresses applied, which depend on the history of the PZT actuators and is not identical between samples. The inset of Fig. 7 shows the normalized loop area for two different ErTe₃ samples in the same configuration. This hysteretic behavior below T_{CDW1} demonstrates that the switching behavior seen in both the elastocaloric and resistivity data represents a first order transition.

Further decreases in temperature cause the loop to close again, then reopen traversing the loop in the counterclockwise direction instead of clockwise. This inversion occurs near T_{CDW2} , although the exact value varies sample to sample.

C. Elastoresistivity

More detailed information can be gleaned by examining the strain derivatives of the resistivity. These quantities can, in principle, be extracted from the resistivity traces presented in Fig. 6. However, we instead used an AC elastoresistivity technique which provides a more sensitive, higher resolution probe of the strain response.[37] The tensor elastoresistivity m_{ijkl} , which relates normalized changes in the resistivity tensor ρ_{ij} to the material strain ε_{kl} is defined as

$$m_{ijkl} = d(\Delta\rho/\rho_0)_{ij}/d\varepsilon_{kl} \quad (7)$$

and has proven a powerful tool in the understanding of symmetry-breaking phase transitions.[39–42] [43]

Figure 8 shows the in-plane, longitudinal elastoresistivity responses in three different samples of ErTe_3 , each under different stress conditions. The most dramatic stress dependence arises for stress and current aligned with the a -axis. The lowest values of V_{outer} , which most closely approximate the case of a freestanding crystal, show two distinct features. The first, near T_{CDW1} , is a sharp dip toward negative elastoresistivity values. As the temperature decreases further, the elastoresistivity grows in magnitude, then shrinks again, resulting in a bulge toward negative values which is separated from the dip at T_{CDW1} by a gentle local maximum.

Increasing the tensile stress causes this larger bulge feature to increase in magnitude. The local maximum becomes less well pronounced. Tensile stresses beyond a certain value of stress (corresponding here to $V_{\text{outer}} \approx 25$ V) the bulge again begins to decrease in size and eventually stabilize for small (≈ -10) elastoresistivity values for the largest stresses. Beyond this critical value of stress, the dip feature at T_{CDW1} inverts to become a small peak which grows as the tensile stress increases.

Elastoresistivity measured along the c -axis, shown in Fig. 8(c) produces qualitatively similar results for the large tensile stress limit of the a -axis elastoresistivity (Fig. 8(a), bottom panel). A small peak appears near T_{CDW1} , which also increases in magnitude for increasing stress. Simultaneously the bulge in the intermediate temperature range also decreases in size.

When stress and current are aligned in the basal plane at 45° to the orthorhombic axes, we observe relatively little response of the resistivity to strain. The peak at T_{CDW1} still appears, and follows a similar trend of increasing with tensile stress. However, no bulge toward negative elastoresistivity values is observed whatsoever.

Figure 9 shows the elastoresistivity measured in TmTe_3 with stress aligned along the a -axis. The phe-

nomenology closely matches that observed ErTe_3 in Fig. 8(a). On the low-tension side, both a relatively sharp dip near T_{CDW1} and a negative bulge at lower temperatures is observed, and for the smallest values of V_{outer} the two are separated by a local maximum. The bulge reaches its largest magnitude at intermediate stresses, then it decreases in size again. The dip near T_{CDW1} also gives way to a positive peak upon crossing this same critical stress value. Beyond the critical stress, the bulge appears to have a sharp change in its slope; below a certain temperature, all of the traces collapse on top of each other.

The positions of the dip or peak near T_{CDW1} , the local maxima for low tension traces, and the minimum of the bulge beyond the critical stress together describe the phase diagram of TmTe_3 in the T - σ_{aa} plane. The results of previous sections allow us to identify the dip (peak) at T_{CDW1} with a transition to a CDW state with wavevector \mathbf{q}_c (\mathbf{q}_a). The features at lower temperature correspond to a second phase transition into a bidirectional CDW state. Altogether, the phase diagram displays the same topology as that produced in Fig. 1(f) by the free energy expansion.

V. DISCUSSION

The combination of thermodynamic and transport results presented here provide compelling evidence of a strain-induced wavevector realignment transition.

A. Elastocaloric effect

We first discuss the elastocaloric effect. The change in behavior in the ECE between freestanding $R\text{Te}_3$ and $R\text{Te}_3$ under a -axis tension can in principle arise from two separate physical effects. Firstly, at temperatures near a general continuous phase transition at temperature T_c , the strength of the critical fluctuations is a function of the reduced temperature $t = (T - T_c)/T_c$. If T_c is tuned adiabatically by an external parameter such as strain, the sample temperature will shift such that the total entropy is conserved. The smaller $|t|$, the larger the change in temperature. The resulting elastocaloric effect is proportional to the critical part of the specific heat $C_p^{(c)}$ and the rate of change of T_c with strain [21, 36]

$$\left(\frac{dT}{d\varepsilon_{ij}}\right)_S = \frac{C_p^{(c)}}{C_p} \frac{dT_c}{d\varepsilon_{ij}} + \dots \quad (8)$$

In $R\text{Te}_3$, we see that the change in sign of the ECE step occurs at the same strain as the change in sign of $dT_{CDW1}/d\varepsilon$, consistent with this relation.

This effect only applies in the fluctuation regime near T_{CDW1} , a region approximately 10-20 K wide in $R\text{Te}_3$. [44] Figure 3 shows that the sign changing behavior of the ECE anomaly (subtracting a linear background)

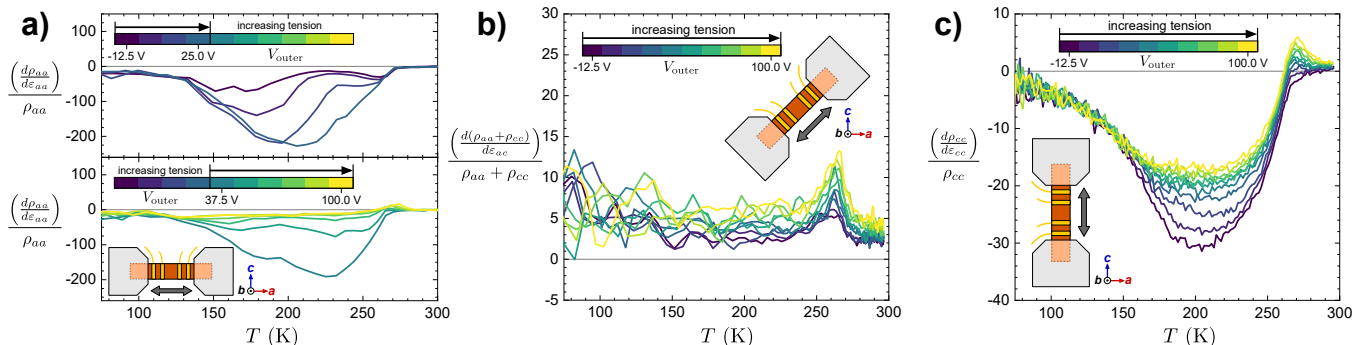


FIG. 8. (a)-(c) Longitudinal elastoresistivity components for ErTe_3 under three different stress orientations, as functions of temperature and PZT voltage. The results from the a -axis sample are split into two subpanels for clarity. Insets describe the orientation of the sample and current in each experiment. In both the a -axis case, increasing tensile strain initially causes the growth of a large negative bulge between approx. 150 K and 265 K, which then increases again for PZT voltages 37.5 V and above. The behavior in the bottom panel of (a) mimics that of (c), where tensile c -axis stress also decreases the magnitude of this negative bulge in the same temperature range. Diagonal stress, as shown in (b), does not generate any such response, indicating that the antisymmetric strain component $\varepsilon_{aa} - \varepsilon_{cc}$ dominates the changes in resistivity. A peak localized at T_{CDW1} appears in all three sample orientations although it carries the opposite sign for compressive and small tensile a -axis stress in the top subpanel of (a). This must therefore arise from the coupling of the CDW order parameter fluctuations to the in-plane symmetric strain or out-of-plane strain.[21]

spans almost 100 K. Well below the transition, the strain dependent ECE must therefore arise from a property of the CDW phase itself, rather than from critical fluctuations. Near the transition, the heat capacity anomalies have been observed to be quite small ($\approx 1\%$ of the total C_p) at both of the CDW transitions in TbTe_3 [45] and ErTe_3 [46]. The derivative of T_{CDW1} with respect to ε_{aa} is approximately 2000 K (Table I), however, such that Eq. (8) predicts an ECE anomaly at T_{CDW1} of approximately 20 K, which is indeed what is observed in both Figs. 3 and 4.

Far from a phase transition, the elastocaloric effect relates to several thermodynamic properties

$$\left(\frac{dT}{d\varepsilon_{ij}}\right)_S = \frac{-T}{C_\sigma} C_{ijkl} \alpha_{kl} \quad (9)$$

where C_σ is the specific heat at constant stress, C_{ijkl} is the elastic constant tensor, and α_{kl} is the thermal expansion tensor. Regardless of the strain in the sample, stability requires that C_σ and C_{ijkl} must retain the same sign, but α_{kl} has no such constraint. Therefore, a strain-induced change in the thermal expansion coefficients could explain the behavior of the ECE in $R\text{Te}_3$.

Previous x-ray measurements[25, 47] have indicated that the antisymmetric in-plane thermal expansion component $\alpha_A = (\alpha_{cc} - \alpha_{aa})/2$ is negative below T_{CDW1} . Ordering of the \mathbf{q}_c CDW therefore reinforces the built-in orthorhombic distortion, increasing the c lattice parameter relative to a . The observed change in sign in the elastocaloric anomaly, and therefore in the thermal expansion, suggests that the CDW wavevector has been switched from parallel to the c -axis to parallel to the a -axis.

B. Resistivity

As the sample traverses this transition, the cross-plane resistivity ρ_{bb} behaves qualitatively the same between T_{CDW1} and T_{CDW2} . This indicates that while the elastocaloric effect indicates a distinct change in electronic anisotropy below T_{CDW1} , a gap of similar magnitude still opens at the Fermi level regardless of the stress conditions. A slight increase is observed in the ρ_{aa} and ρ_{cc} components just below T_{CDW1} as well, again regardless of stress. The suppression of the gap-induced increase in ρ_{aa} with increasing σ_{aa} further supports the inverted electronic anisotropy observed in the elastocaloric effect. These observations support the theory that while the wavevector is realigned from \mathbf{q}_c to \mathbf{q}_a , the overall structure of the new CDW phase does not change appreciably.

As mentioned above, the hysteretic response of ρ_{aa} indicates that the $\mathbf{q}_c \leftrightarrow \mathbf{q}_a$ transition is first order, as should be expected by symmetry if there is no intervening coexistence region. Interestingly, the hysteresis loop closes again at lower temperatures. A possible explanation for this is evident in the sixth-order free energy expansion presented in Section II and Fig. 1(f). On either side of the first order transition, the region of metastability is bounded by a curve which starts at one of the multicritical points and ends at the other. In this model, the metastable region has the largest width along the stress axis at the temperature halfway between these points, and shrinks in width approaching either point. At the lower critical point, the transitions once again become second order in this model.

In practice, the wavevectors of the two separate CDWs are known to differ slightly in magnitude.[22, 48] This detail, which is not included in the phenomenological model

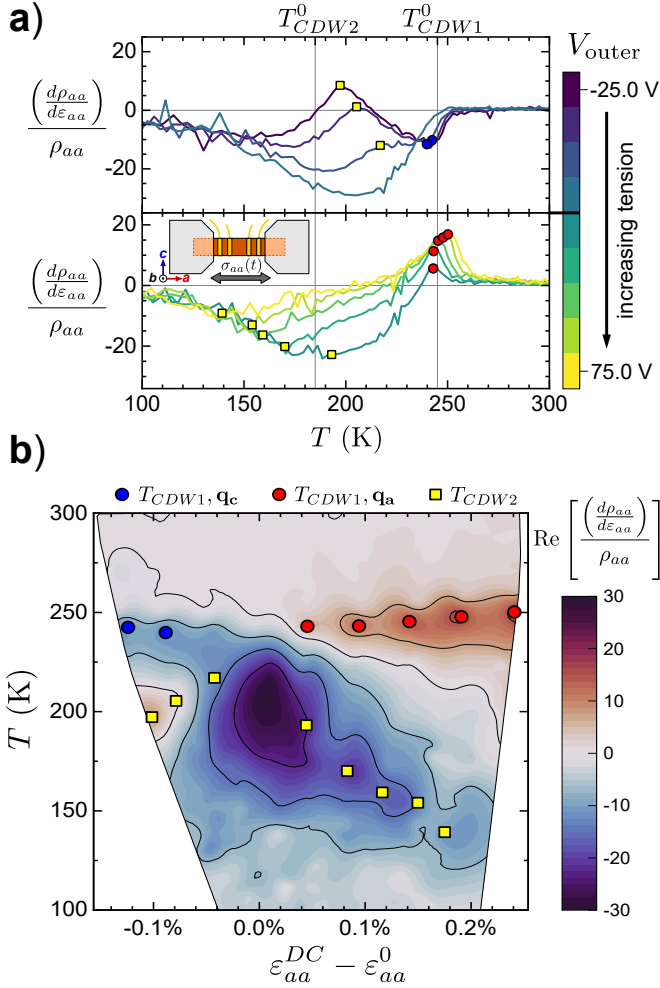


FIG. 9. Longitudinal a -axis elastoresistivity in TmTe_3 . Data presented here was taken by stepping the PZT voltage while sweeping temperature and extracted for steps of increasing tension only. (a) Elastoresistivity as a function of temperature and PZT voltage. Traces are all from the same sample, but have been separated into two panels for clarity. The top panel contains the responses for the most compressive/least tensile stress conditions, and the bottom for the largest tensile stresses. (b) The same data as in (a) presented in the strain-temperature plane. Symbols correspond to the extracted extrema in the traces in (a). The extracted phase transitions, in conjunction with the evidence for a first order transition as shown in Fig. 7, maps directly onto the phase diagram presented in Fig. 1(f).

presented above, would require the presence of a first order transition below the lower critical point inside the checkerboard phase. This transition would correspond to an alteration whether the CDW wavevector parallel to c or a is dominant, although both order parameters would always be nonzero. Hysteresis at low temperatures likely corresponds to such a transition.

The inverted direction of the low temperature hysteresis loop would be a simple consequence of the antisymmetric strain. For example, tensile stress σ_{aa} appears

to stabilize the gap corresponding to ψ_{aa} and weaken the gap corresponding to ψ_{cc} . The c -axis gap affects ρ_{aa} more strongly[30], but both gaps do still cause the resistivity to increase due to loss of density of states. Below T_{CDW2} and under tensile stress, the gap at \mathbf{q}_a is well-established and less sensitive to strain, while the secondary gap at \mathbf{q}_c is small and highly sensitive. Therefore an *increase* in σ_{aa} will *decrease* ψ_c , leading to a *decrease* in the resistivity, which matches the observed orientation of the hysteresis loop at low temperatures.

C. Elastoresistivity

Orthorhombic symmetry groups, such as that found in $R\text{Te}_3$, impose very few constraints on the coupling between CDW phases and uniform strain ε_{ij} with wavevectors along the principle axes. Consider a generalized coupling of the form $\varepsilon_{ij}\Lambda_{ijk}|\psi_k|^2$, where $k = a, c$. The crystal structure dictates that $\Lambda_{ijk} = 0$ for $i = j$, but the six remaining components may be arbitrary. In the tetragonal limit, one may take $\Lambda_{iik} = \Lambda_{kki}$. However, as uniaxial stress experiments generate nonzero values for several ε_{ii} components, disentangling the effects of each on the CDW is not trivial.

Despite this general complexity, the phenomenology of $R\text{Te}_3$ under uniaxial stress is remarkably simple. Specifically, the three elastoresistivity components presented in Fig. 8 allow us to identify the in-plane antisymmetric component of the strain, $\varepsilon_A = (\varepsilon_{aa} - \varepsilon_{cc})/2$, as the operative tuning parameter for the strain-induced transitions. Furthermore, the in-plane symmetric component $\varepsilon_S = (\varepsilon_{aa} + \varepsilon_{cc})/2$ and the out-of-plane component ε_{bb} only contribute to shifts in critical temperature.

To see this, consider first the a - and c -axis elastoresistivity measurements. Both show similar phenomenology below T_{CDW1} under large tensile stress. Except for a small anisotropy in the elastic constants, these measurements are performed under similar magnitudes of ε_S , ε_{bb} and ε_A , although the sign of ε_A will be flipped. In contrast, applying uniaxial stress along the in-plane diagonal results in $\varepsilon_A \approx 0$ and $\varepsilon_{ac} \neq 0$. The symmetric components ε_S and ε_{bb} will again be similar. Because ε_{ac} can only couple to the CDW at quadratic or higher order, this diagonal configuration effectively only probes the response to symmetric strains.

The large negative elastoresistivity response present in the a - and c -axis configurations can then only arise from coupling to ε_A . All three experiments showed evidence of a peak (or dip) near T_{CDW1} ; this effect must then arise from coupling to the symmetric strains. By similar arguments as made above in developing Eq. (8), it can be shown that near a strain-tuned continuous phase transition, the elastoresistivity will also display similar singular behavior to the heat capacity.[21] We can therefore identify the peak as arising from changes in T_{CDW1} caused by the ε_S and ε_{bb} .

Extracted values of the change in critical temperatures

TABLE I. Rate of change of the critical temperatures T_{CDW1} and T_{CDW2} with strain in the strain-induced \mathbf{q}_a state. In all of these experiments, uniaxial stress is applied long the a -axis. Not all techniques are sensitive to T_{CDW2} . The strain range of the ρ_{bb} measurements was insufficient to observe consistent linear behavior in T_{CDW1} . Sources of sample-to-sample variation are described in the text.

		$\frac{dT_{CDW1}}{d\varepsilon_{aa}}$ (K)	$\frac{dT_{CDW2}}{d\varepsilon_{aa}}$ (K)
ErTe ₃	ECE	4650 ± 1130	.
	ρ_{aa}	6840 ± 670	.
	ρ_{bb}	.	-13000 ± 1620
TmTe ₃	ECE	2210 ± 576	.
	ρ_{aa}	5150 ± 674	.
	ER	4370 ± 977	-22100 ± 3900

for the strain-induced \mathbf{q}_a state under strain are presented in Table I. In general, the T_{CDW2} is seen to be approximately 3-5 times more sensitive to strain than T_{CDW1} . The relatively large scatter in the different measurement techniques likely arises from uncertainty in the strain transmission from the stress cell to the sample, as well as run-to-run variations. Possible sources of sample-to-sample differences arise from differences the thickness of the epoxy layer used for mounting and uncertainties in the spacing between the mounting plates. Additionally, near the critical point the predicted sharp cusp in T_{CDW1} is seen to be rounded somewhat, likely due to strain inhomogeneities in the sample. This curvature can also lead to an underestimate of $dT_{CDW1}/d\varepsilon_{aa}$. However, if we assuming a Young's modulus E of approximately 50 GPa[49], these values are all consistent with the range of values of $dT_{CDW1}/d\sigma_{aa} = E^{-1}(dT_{CDW1}/d\varepsilon_{aa})$ previously reported for several $R\text{Te}_3$ compounds.[45, 46, 50]

VI. CONCLUSIONS

In this work, we have shown that $R\text{Te}_3$, specifically ErTe_3 and TmTe_3 , provide a practical model system for the study of strain-CDW interactions. In particular, uniaxial stress can tune $R\text{Te}_3$ to and beyond a quasi-tetragonal state for which the CDW wavevector realigns along the a -axis rather than the c -axis. Through thermodynamic and transport measurements, we have established a phase diagram and identified several phase transitions; a second order transition to the \mathbf{q}_a -only state upon cooling under uniaxial stress, and a first-order transition between the \mathbf{q}_c and \mathbf{q}_a states induced by uniaxial stress for temperatures below T_{CDW1} . This work motivates the application of x-ray scattering and ARPES studies of $R\text{Te}_3$ under strain to further quantify the behavior and characteristics of the strain-induced \mathbf{q}_a state. More broadly, extension of the techniques presented here to samples with quenched disorder, such as Pd_xRTe_3 [51, 52] may also provide unique insight into frustrated charge order on a tetragonal lattice under uniaxial stress. More broadly, This work provides guiding principles for the study of the general behavior of unidirectional CDW phases and lays the foundation for future, more specialized explorations.

VII. ACKNOWLEDGMENTS

The authors wish to thank Steve Kivelson for insightful discussions. This work was supported by the United States Department of Energy, Office of Basic Sciences, under Contract No. DE-AC02-76SF00515. Part of this work was performed at the Stanford Nano Shared Facilities (SNSF)/Stanford Nanofabrication Facility (SNF), supported by the National Science Foundation under award ECCS-1542152.

-
- [1] W. Tabis, Y. Li, M. L. Tacon, L. Braicovich, A. Kreyssig, M. Minola, G. Dellea, E. Weschke, M. J. Veit, M. Ramazanoglu, A. I. Goldman, T. Schmitt, G. Ghiringhelli, N. Barišić, M. K. Chan, C. J. Dorow, G. Yu, X. Zhao, B. Keimer, and M. Greven, *Nat. Commun.* **5**, 5875 (2014).
 - [2] R. Comin, R. Sutarto, F. He, E. H. da Silva Neto, L. Chauviere, A. Fraño, R. Liang, W. N. Hardy, D. A. Bonn, Y. Yoshida, H. Eisaki, A. J. Achkar, D. G. Hawthorn, B. Keimer, G. A. Sawatzky, and A. Damascelli, *Nat. Mater.* **14**, 796 (2015).
 - [3] S. Gerber, H. Jang, H. Nojiri, S. Matsuzawa, H. Yasumura, D. A. Bonn, R. Liang, W. N. Hardy, Z. Islam, A. Mehta, S. Song, M. Sikorski, D. Stefanescu, Y. Feng, S. A. Kivelson, T. P. Devereaux, Z. X. Shen, C. C. Kao, W. S. Lee, D. Zhu, and J. S. Lee, *Science* **350**, 949 (2015).
 - [4] H. Jang, W.-S. Lee, H. Nojiri, S. Matsuzawa, H. Yasumura, L. Nie, A. V. Maharaj, S. Gerber, Y.-J. Liu, A. Mehta, D. A. Bonn, R. Liang, W. N. Hardy, C. A. Burns, Z. Islam, S. Song, J. Hastings, T. P. Devereaux, Z.-X. Shen, S. A. Kivelson, C.-C. Kao, D. Zhu, and J.-S. Lee, *Proc. Natl. Acad. Sci. U. S. A.* **113**, 14645 (2016).
 - [5] J.-J. Wen, H. Huang, S.-J. Lee, H. Jang, J. Knight, Y. S. Lee, M. Fujita, K. M. Suzuki, S. Asano, S. A. Kivelson, C.-C. Kao, and J.-S. Lee, *Nat. Commun.* **10**, 3269 (2019).
 - [6] S. K. Chan and V. Heine, *J. Phys. F Met. Phys.* **3**, 795 (1973).
 - [7] H. Requardt, J. E. Lorenzo, P. Monceau, R. Currat, and M. Krisch, *Phys. Rev. B* **66**, 214303 (2002).
 - [8] M. Leroux, I. Errea, M. Le Tacon, S.-M. Souliou, G. Garbarino, L. Cario, A. Bosak, F. Mauri, M. Calandra, and P. Rodière, *Phys. Rev. B* **92**, 140303 (2015).

- [9] M. Maschek, S. Rosenkranz, R. Hott, R. Heid, M. Merz, D. A. Zocco, A. H. Said, A. Alatas, G. Karapetrov, S. Zhu, J. Van Wezel, and F. Weber, *Phys. Rev. B* **94**, 1 (2016).
- [10] M. Maschek, D. A. Zocco, S. Rosenkranz, R. Heid, A. H. Said, A. Alatas, P. Walmsley, I. R. Fisher, and F. Weber, *Phys. Rev. B* **98**, 094304 (2018).
- [11] M. D. Johannes and I. I. Mazin, *Phys. Rev. B* **77**, 165135 (2008).
- [12] J. J. Hamlin, D. A. Zocco, T. A. Sayles, M. B. Maple, J. H. Chu, and I. R. Fisher, *Phys. Rev. Lett.* **102**, 177002 (2009).
- [13] A. Soumyanarayanan, M. M. Yee, Y. He, J. V. Wezel, D. J. Rahn, K. Rossnagel, E. W. Hudson, M. R. Norman, and J. E. Hoffman, *Proc. Natl. Acad. Sci. U. S. A.* **110**, 1623 (2013).
- [14] F. Flicker and J. Van Wezel, *Phys. Rev. B* **92**, 1 (2015).
- [15] D. A. Zocco, J. J. Hamlin, K. Grube, J.-H. Chu, H.-H. Kuo, I. R. Fisher, and M. B. Maple, *Phys. Rev. B* **91**, 205114 (2015).
- [16] S. Lei, J. Lin, Y. Jia, M. Gray, A. Topp, G. Farahi, S. Klemen, T. Gao, F. Rodolakis, J. L. McChesney, C. R. Ast, A. Yazdani, K. S. Burch, S. Wu, N. P. Ong, and L. M. Schoop, *Sci. Adv.* **6**, eaay6407 (2020).
- [17] L. Nie, G. Tarjus, and S. A. Kivelson, *Proc. Natl. Acad. Sci. U. S. A.* **111**, 7980 (2014).
- [18] R. M. Fernandes, S. A. Kivelson, and E. Berg, *Phys. Rev. B* **93**, 014511 (2016).
- [19] L. Nie, A. V. Maharaj, E. Fradkin, and S. A. Kivelson, *Phys. Rev. B* **96**, 085142 (2017).
- [20] R. M. Fernandes, P. P. Orth, and J. Schmalian, *Annu. Rev. Condens. Matter Phys.* **10**, 133 (2019).
- [21] A. T. Hristov, M. S. Ikeda, J. C. Palmstrom, P. Walmsley, and I. R. Fisher, *Phys. Rev. B* **99**, 100101 (2019).
- [22] A. Banerjee, Y. Feng, D. M. Silevitch, J. Wang, J. C. Lang, H. H. Kuo, I. R. Fisher, and T. F. Rosenbaum, *Phys. Rev. B* **87**, 155131 (2013).
- [23] W. L. McMillan, *Phys. Rev. B* **12**, 1187 (1975).
- [24] C. D. Malliakas and M. G. Kanatzidis, *J. Am. Chem. Soc.* **128**, 12612 (2006).
- [25] N. Ru, C. L. Condron, G. Y. Margulis, K. Y. Shin, J. Laverock, S. B. Dugdale, M. F. Toney, and I. R. Fisher, *Phys. Rev. B* **77**, 035114 (2008).
- [26] A. Fang, N. Ru, I. R. Fisher, and A. Kapitulnik, *Phys. Rev. Lett.* **99**, 046401 (2007).
- [27] L. Fu, A. M. Kraft, B. Sharma, M. Singh, P. Walmsley, I. R. Fisher, and M. C. Boyer, *Phys. Rev. B* **94**, 205101 (2016).
- [28] U. Ralević, N. Lazarević, A. Baum, H. M. Eiter, R. Hackl, P. Giraldo-Gallo, I. R. Fisher, C. Petrovic, R. Gajić, and Z. V. Popović, *Phys. Rev. B* **94**, 1 (2016).
- [29] N. Ru and I. R. Fisher, *Phys. Rev. B* **73**, 033101 (2006).
- [30] A. A. Sinchenko, P. D. Grigoriev, P. Lejay, and P. Monceau, *Phys. Rev. Lett.* **112**, 036601 (2014).
- [31] N. Ru, R. A. Borzi, A. Rost, A. P. Mackenzie, J. Laverock, S. B. Dugdale, and I. R. Fisher, *Phys. Rev. B* **78**, 045123 (2008).
- [32] P. D. Grigoriev, A. A. Sinchenko, P. Lejay, A. Hadj-Azzem, J. Balay, O. Leynaud, V. N. Zverev, and P. Monceau, *Eur. Phys. J. B* **89**, 151 (2016).
- [33] H. Yao, J. A. Robertson, E. A. Kim, and S. A. Kivelson, *Phys. Rev. B* **74**, 1 (2006).
- [34] A. Fang, J. A. W. Straquadine, I. R. Fisher, S. A. Kivelson, and A. Kapitulnik, *Phys. Rev. B* **100**, 235446 (2019).
- [35] M. S. Ikeda, T. Worasaran, J. C. Palmstrom, J. A. W. Straquadine, P. Walmsley, and I. R. Fisher, *Phys. Rev. B* **98**, 245133 (2018).
- [36] M. S. Ikeda, J. A. W. Straquadine, A. T. Hristov, T. Worasaran, J. C. Palmstrom, M. Sorensen, P. Walmsley, and I. R. Fisher, *Rev. Sci. Instrum.* **90**, 083902 (2019).
- [37] A. T. Hristov, J. C. Palmstrom, J. A. W. Straquadine, T. A. Merz, H. Y. Hwang, and I. R. Fisher, *Rev. Sci. Instrum.* **89**, 103901 (2018).
- [38] P. Walmsley and I. R. Fisher, *Rev. Sci. Instrum.* **88**, 043901 (2017).
- [39] J.-H. Chu, H.-H. Kuo, J. G. Analytis, and I. R. Fisher, *Science* **337**, 710 (2012).
- [40] S. C. Riggs, M. C. Shapiro, A. V. Maharaj, S. Raghu, E. D. Bauer, R. E. Baumbach, P. Giraldo-Gallo, M. Wartenbe, and I. R. Fisher, *Nat. Commun.* **6**, 6425 (2014).
- [41] H.-H. Kuo, J.-H. Chu, J. C. Palmstrom, S. A. Kivelson, and I. R. Fisher, *Science* **352**, 958 (2016).
- [42] E. W. Rosenberg, J.-H. Chu, J. P. C. Ruff, A. T. Hristov, and I. R. Fisher, *Proc. Natl. Acad. Sci. U. S. A.* **116**, 7232 (2019).
- [43] The normalizing resistivity ρ_0 is usually taken as the geometric mean of the relevant resistivity tensor components at zero strain.[53] However, due to large ($\approx 20\%$) changes in the resistivity as shown in Fig. 6(b), we elect instead to normalize by the simultaneously measured resistivity. This allows us to present our data without making any ancillary measurements or extrapolations.
- [44] H.-M. Eiter, M. Lavagnini, R. Hackl, E. A. Nowadnick, A. F. Kemper, T. P. Devereaux, J.-H. Chu, J. G. Analytis, I. R. Fisher, and L. Degiorgi, *Proc. Natl. Acad. Sci. U. S. A.* **110**, 64 (2013).
- [45] M. Saint-Paul, C. Guttin, P. Lejay, G. Remenyi, O. Leynaud, and P. Monceau, *Solid State Commun.* **233**, 24 (2016).
- [46] M. Saint-Paul, G. Remenyi, C. Guttin, P. Lejay, and P. Monceau, *Phys. B Condens. Matter* **504**, 39 (2017).
- [47] A. Sacchetti, C. L. Condron, S. N. Gvasaliya, F. Pfanner, M. Lavagnini, M. Baldini, M. F. Toney, M. Merlini, M. Hanfland, J. Mesot, J. H. Chu, I. R. Fisher, P. Postorino, and L. Degiorgi, *Phys. Rev. B* **79**, 4 (2009).
- [48] A. Kogar, A. Zong, P. E. Dolgirev, X. Shen, J. Straquadine, Y.-Q. Bie, X. Wang, T. Rohwer, I.-C. Tung, Y. Yang, R. Li, J. Yang, S. Weathersby, S. Park, M. E. Kozina, E. J. Sie, H. Wen, P. Jarillo-Herrero, I. R. Fisher, X. Wang, and N. Gedik, *Nat. Phys.* **16**, 159 (2020).
- [49] M. Saint-Paul and P. Monceau, *Adv. Condens. Matter Phys.* **2019**, 1 (2019).
- [50] M. Saint-Paul, C. Guttin, P. Lejay, O. Leynaud, and P. Monceau, *Int. J. Mod. Phys. B* **32**, 1 (2018).
- [51] J. A. W. Straquadine, F. Weber, S. Rosenkranz, A. H. Said, and I. R. Fisher, *Phys. Rev. B* **99**, 235138 (2019).
- [52] R. Lou, Y. Cai, Z. Liu, T. Qian, L. Zhao, Y. Li, K. Liu, Z. Han, D. Zhang, J. He, G. Chen, H. Ding, and S. Wang, *Phys. Rev. B* **93**, 115133 (2016).
- [53] M. C. Shapiro, P. Hlobil, A. T. Hristov, A. V. Maharaj, and I. R. Fisher, *Phys. Rev. B* **92**, 235147 (2015).
- [54] Keysight, *Impedance Measurement Handbook: A guide to measurement technology and techniques*, 6th ed. (2016).

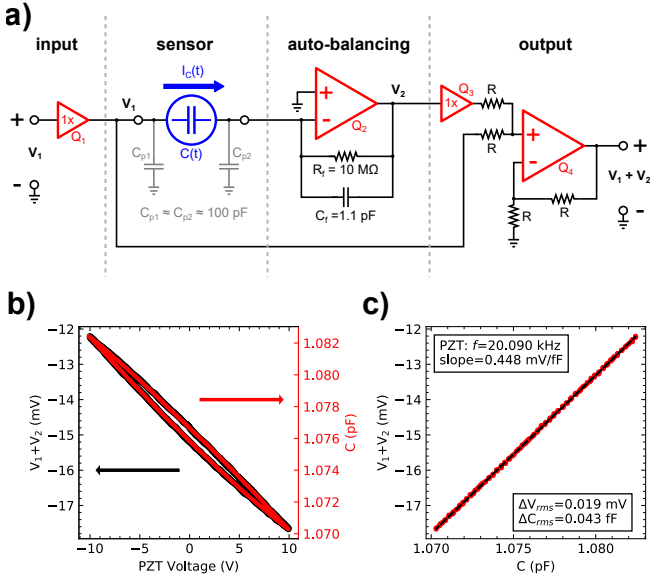


FIG. 10. Construction and calibration of the auto-balancing capacitance bridge. (a) Diagram of the circuit employed here. A ≈ 20 kHz reference input sine wave (V_1) is buffered at the input, then applied to one terminal of the displacement sensor through coaxial cables. The opposite terminal is connected to a virtual ground by the auto-balancing section, where the feedback capacitor acts as a reference. The output V_2 of the auto-balancing bridge will be a sine wave with magnitude proportional to the ratio of the sensor and reference capacitances, but 180° out of phase with the reference. The signal at V_1 and V_2 are added together with a non-inverting summing amplifier, and the two will cancel if the sensor and reference capacitances are equal. (b) Output of the capacitance bridge (right axis) overlaid with independent quasistatic measurements made with a commercial capacitance bridge. (c) The output voltage plotted against the measured capacitance, demonstrating linear behavior and a sensitivity of $448 \mu\text{V}/\text{fF}$ and a root-mean-square noise floor of 43 aF. This corresponds to a displacement of approximately 2 nm.

Appendix A: AC capacitance measurements

The CS-100 uniaxial strain cell from *Razorbill Instruments* incorporates a capacitive displacement sensor used to quantify the strain in the sample. Highly accurate measurements of the capacitance can be made for quasi-static cell displacements, but techniques for measuring changes in capacitance occurring at frequencies above a few Hz are not well established. To make it possible to accurately quantify the oscillating strains, and therefore of the elastoresistivity and elastocaloric effect, we have developed a custom bridge circuit (based on a commonly used impedance measurement technique[54]) which, in conjunction with a pair of lock-in amplifiers, measures both DC and AC changes in capacitance. The bridge is based on an auto-balancing bridge topology, which can effectively cancel effects of parasitic capacitances due to the cables.

A simplified circuit schematic is shown in Fig. 10. An AC voltage (amplitude 0.5 V, frequency around 20 kHz) is applied to the input terminal, passed through a unity-gain buffer Q_1 to minimize the output impedance, and then passed to the CS-100 displacement sensor through a coaxial cable. The capacitance of the sensor is of order 1 pF and varies approximately ± 250 fF through the full range of displacements. In comparison, typical capacitances for the coaxial cables required to connect the circuit (at room temperature) to the stress cell inside the cryostat are of order 100 pF, more than two orders of magnitude larger than the changes to be observed. The low output impedance of the first buffer stage prevents phase lag due to charging and discharging of this parasitic cable capacitance C_{p1} .

The other terminal of the capacitive sensor is connected to a virtual ground at the inverting terminal of the auto-balancing stage. The feedback network of this stage contains capacitor which acts as the reference, as well as a resistor for stability. The output of this stage is such that the second terminal of the capacitive sensor remains at zero volts, implying that the parasitic capacitance C_{p2} at this terminal does not draw any current. The output voltage V_2 required for this is proportional to the ratio of the sensor capacitance $C(t)$ to the reference capacitance C_f , but with opposite sign. The final stage combines the output V_2 with the input reference signal such that the two cancel exactly when $C(t) = C_f$.

The magnitude of the sum is detected by a lock-in amplifier. Knowing C_f , the time-averaged magnitude can then be converted to provide a measurement of the DC capacitance. The instantaneous magnitude as it appears at the output of the lock-in amplifier, however still contains the modulation at the strain frequency; a second demodulation stage of this signal provides direct access to the magnitude of the AC capacitance variation.

We have calibrated our bridge circuit against a commercial capacitance bridge for quasi-static strain, as shown in Fig. 10(b) and (c), and found that the behavior is well within the linear regime. The capacitance-to-voltage conversion factor is approximately 0.448 mV/fF, and the noise floor is approximately 43 aF. By simulating the strain-modulated capacitance sensor with an amplitude-modulated current source, we have also confirmed that the circuit described here maintains its accuracy to within 2% for strain frequencies up to 1 kHz.

Typical changes in capacitance for a $5 V_{\text{rms}}$ oscillating voltage on the outer pair of piezoelectric stacks range between 0.75 fF at 20 K to approximately 2.5 fF $_{\text{rms}}$ at room temperature.

Appendix B: Frequency dependence of ECE measurements

As described in detail in ref. 36, the criteria for quasi-adiabatic behavior in ECE measurements depend on the thermal properties of the sample, as well as the properties

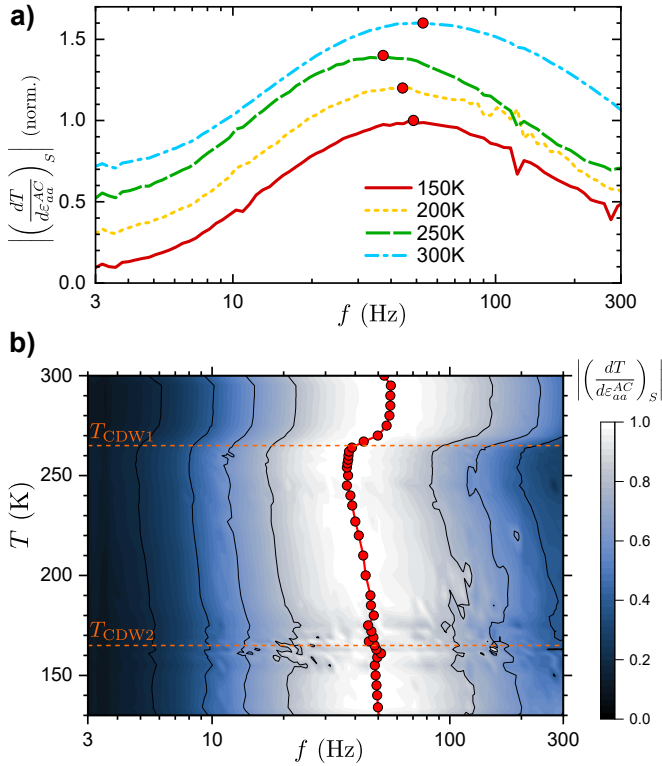


FIG. 11. Frequency dependence of elastocaloric effect measurements on ErTe_3 under a -axis stress. (a) Magnitude of the ECE signal as a function of strain frequency for several representative temperatures. Each curve is normalized to the maximum signal observed at that temperature, and the curves are vertically offset for clarity. The peak is notated with a red circle. Panel (b) shows similar data for a dense set of temperatures, presented as a contour plot. As the sample cools below T_{CDW1} , the peak frequency decreases from approximately 55 Hz to approximately 35 Hz. This shift in the peak frequency reflects a sudden decrease in thermal conductivity. This is consistent with the Wiedemann-Franz law: this measurement is most sensitive to the thermal conductivity along the a -axis, and the electrical resistivity ρ_{aa} also shows the highest increase when cooling through T_{CDW1} . Data presented in the main text was acquired for a constant frequency in the range of 20 – 40 Hz. Shifts in the frequency dependence with temperature will affect the absolute magnitudes of the ECE signals in Figs. 3 and 4, but would alter neither qualitative behavior nor the conclusions stemming from this data.

of the materials used to mount the sample and to adhere the thermocouple. At low strain frequencies, the sample tends to thermalize with the mounting plates, decreasing the observed temperature oscillation magnitude. At high strain frequencies, the thermocouple can no longer follow the changes in temperature. The maximum signal is observed at intermediate frequencies. Formally, the low frequency cutoff for quasi-adiabatic behavior ω_{qa}

depends on the thermal conductivity κ , the volumetric specific heat ρc_p , and the sample length L as

$$\omega_{qa} \propto \frac{\kappa}{\rho c_p L^2}. \quad (\text{B1})$$

As a consequence, any changes in the thermal conductivity or specific heat will result in a change of the observed elastocaloric signal.

Upon cooling, as one passes through the CDW transition temperature T_{CDW1} , the electrical resistivity is shown in Fig. 6 to change significantly, especially ρ_{aa} . The Wiedemann-Franz law suggests that a similar change would be observed in the thermal conductivity. The temperature dependence data presented in Figs. 3 and 4 was taken using a single frequency for the entire temperature and strain range; the temperature dependence of the thermal conductivity should be expected to alter the signal.

Figure 11 shows the frequency dependence of magnitude of the elastocaloric effect for a -axis stress on ErTe_3 as a function of temperature. The frequency f_p at which the ECE reaches its peak is denoted by the filled symbols. As the sample is cooled through T_{CDW1} , the location of the maximum moves to lower frequencies, corresponding to a change in the ratio κ/c_p . The heat capacity, which is dominated by the phonon background (the Debye temperature $\Theta_D \approx 180$ K[22, 29]) is known to be approximately constant through T_{CDW1} [46]. Therefore the change in the frequency dependence must arise from changes in the thermal conductivity.

Two different contributions to the ECE anomaly at T_{CDW1} were discussed in the main text: critical fluctuations near a strain-tuned phase transition, and changes in the thermal expansion tensor. For an ECE measurement at a constant frequency f_0 , however, a sharp change in the frequency dependence can also contribute to this anomaly. If $f_0 < f_p$, the frequency dependence would cause the ECE magnitude to rise upon cooling through T_{CDW1} . The ECE measurements in Figs. 3 and 4 were made with strain frequencies of 37 Hz and 51 Hz, respectively. The ECE anomaly in the near-freestanding case does indeed increase the ECE magnitude on cooling through T_{CDW1} , implying that a frequency dependence could indeed be contributing to the behavior. However, both the \mathbf{q}_c and strain-induced \mathbf{q}_a states should correspond to a decrease in thermal conductivity due to the opening of a CDW gap. Therefore we conclude that changes in the frequency dependence can decrease the size of the ECE anomaly, but such changes cannot explain the change in sign of the anomaly. Frequency dependent effects can at most alter the absolute magnitude, but the effects discussed in the main text must still be the primary contributions to the ECE.